



HAL
open science

Strain localization in circular honeycombs under in-plane biaxial quasi-static and low velocity impact loading

D. Karagiozova, T.X. Yu

► **To cite this version:**

D. Karagiozova, T.X. Yu. Strain localization in circular honeycombs under in-plane biaxial quasi-static and low velocity impact loading. *International Journal of Impact Engineering*, 2008, 35 (8), pp.753. 10.1016/j.ijimpeng.2007.11.001 . hal-00499106

HAL Id: hal-00499106

<https://hal.science/hal-00499106>

Submitted on 9 Jul 2010

HAL is a multi-disciplinary open access archive for the deposit and dissemination of scientific research documents, whether they are published or not. The documents may come from teaching and research institutions in France or abroad, or from public or private research centers.

L'archive ouverte pluridisciplinaire **HAL**, est destinée au dépôt et à la diffusion de documents scientifiques de niveau recherche, publiés ou non, émanant des établissements d'enseignement et de recherche français ou étrangers, des laboratoires publics ou privés.

Author's Accepted Manuscript

Strain localization in circular honeycombs under in-plane biaxial quasi-static and low velocity impact loading

D. Karagiozova, T.X. Yu

PII: S0734-743X(07)00182-0
DOI: doi:10.1016/j.ijimpeng.2007.11.001
Reference: IE 1538

To appear in: *International Journal of Impact*

Received date: 25 May 2007
Revised date: 14 November 2007
Accepted date: 15 November 2007

Cite this article as: D. Karagiozova and T.X. Yu, Strain localization in circular honeycombs under in-plane biaxial quasi-static and low velocity impact loading, *International Journal of Impact* (2007), doi:10.1016/j.ijimpeng.2007.11.001

This is a PDF file of an unedited manuscript that has been accepted for publication. As a service to our customers we are providing this early version of the manuscript. The manuscript will undergo copyediting, typesetting, and review of the resulting galley proof before it is published in its final citable form. Please note that during the production process errors may be discovered which could affect the content, and all legal disclaimers that apply to the journal pertain.



www.elsevier.com/locate/ijimpeng

**Strain localization in circular honeycombs
under in-plane biaxial quasi-static and low velocity impact loading**

D. Karagiozova^{a,b*} and T.X. Yu^b

^a*Institute of Mechanics, Bulgarian Academy of Sciences,
Acad. G. Bonchev Street, Block 4, Sofia 1113, Bulgaria*

^b*Department of Mechanical Engineering, The Hong Kong University of Science and Technology,
Clear Water Bay, Kowloon, Hong Kong*

Abstract

The strain localization in a finite block of circular honeycomb is studied using a phenomenological approach based on the structural response of the honeycombs. The deformation modes characteristic for a circular honeycomb material under in-plane biaxial compression are identified from the experiments and described analytically for compression strains up to about 15%. It is concluded that the particular deformation modes depend on the local strain field and modes with different dominant strains can co-exist inside a finite block subjected to equi-biaxial remote strains. The relationships between the local strain components for the development of these modes are determined. Using the proposed approach to the strain localisation, it is shown that for equal remote strains applied to a finite block of honeycombs, larger remote stresses would occur when assuming homogeneous deformation inside the block in comparison to the calculated stress when the strain inhomogeneity takes place. A comparison between the theoretical and experimental results is made for a finite honeycomb block under quasi-static equi-biaxial compression.

Key words – Circular honeycomb; Biaxial compression; Strain localisation, Deformation modes; Non-linear elastic material

* Corresponding author: Fax: +359 2870 7498
E-mail: d.karagiozova@imbm.bas.bg

Nomenclature

a, b	major and minor semi-axis of an ellipse
d_x, d_y	initial dimensions of a representative block having 2×2 cells
$E(\varepsilon)$	elastic modulus for a non-linear elastic material
F_x, F_y	components of the remote force applied to a representative block of 2×2 cells
F_X, F_Y	force components of the applied load to the finite honeycomb block
$g(\mu)$	parameter depending on friction
H	depth of a honeycomb block
L_X, L_Y	dimensions of a finite honeycomb block
p_{el}	perimeter of an ellipse
r_{el}	current radius of curvature of an ellipse
R, t	radius of a circular cell and thickness of the cell wall, respectively
U_{el}, W	internal and external energies defined for a 2×2 cells block per unit depth of the block
V_0	applied constant velocity to the moving arms of the loading device
V_X, V_Y	velocity components at the interface related to the finite honeycomb block
$\dot{W}_e, \dot{W}_i, \dot{W}_f$	external, internal and frictional power, respectively, related to the finite honeycomb block
x, y	coordinates with respect to a 2×2 cells block
$x_{i,j}, y_{i,j}$	current coordinates of rectangular blocks inside the finite block
X, Y	global coordinates with respect to the finite block and loading device
z	coordinate across the cell wall thickness
δ_x, δ_y	displacements of the representative block having 2×2 cells
$\bar{\delta}_x', \bar{\delta}_y'$	dimensionless displacements (local coordinate system) of the representative block having 2×2 cells
δ_X, δ_Y	displacements in the finite honeycomb block at the interface with the loading device
$\delta_x^{ij}, \delta_y^{ij}$	displacements of the 2×2 cells blocks within the finite block
Δ_X, Δ_Y	displacements of the moving arms of the loading device
$\varepsilon(z)$	bending strain in a cell wall
$\varepsilon_x, \varepsilon_y$	remote strains of a representative block having 2×2 cells
$\varepsilon_x^{ij}, \varepsilon_y^{ij}$	remote strains for a 2×2 cells block inside the finite block
$\varepsilon_X, \varepsilon_Y$	average strains of the finite honeycomb block
ρ, ρ^*	density of the cell wall material and density of the honeycomb material, respectively
σ_x, σ_y	remote stresses for a 2×2 cells block
σ_X, σ_Y	remote stresses for the finite honeycomb block
$\sigma_w(\varepsilon)$	material characteristic of the cell wall

1 Introduction

The experimental and theoretical analyses of the response of cellular materials to various types of loading are important for understanding the properties of these materials, which have a wide range of engineering applications [1]. The biaxial crushing of cellular materials, in particular, is quite complex to perform experimentally so that only a few experimental studies have been reported in the literature. The biaxial crushing device, which was designed to study the stress-strain characteristics of hexagonal honeycombs and described by Papka and Kyriakides [2,3], allowed movements of all four arms, while the biaxial crushing of circular honeycombs reported by Chung and Waas [4-6] was performed as a constrained uniaxial compression (static and dynamic). In both cases various deformation patterns (modes) are observed and they are related to the particular ratio between the components of the applied displacements or forces. It is noticeable, however, that a mixture of deformation modes was observed, particularly when an equi-biaxial compression was applied [2], although particular modes were theoretically associated with this loading. One reason is that the influence of the boundaries of the tested block cannot be neglected. Another reason is related to the strain localisations, which ‘destroy’ the homogeneity of deformation.

Materials with regular structure can exhibit structural instability effects (buckling) at the meso-scale (scale of the cells), which can cause material instability effects (localization) in the macro-scale. According to a number of studies reported recently in the literature [7-9], strain localization that occurs in a block of material with open cells having a regular structure, honeycomb [7,8] and a lattice structure (Kelvin cells) [9], is attributed to the existence of doubly-scaled deformation. One is related to the bifurcation independent on the number of cells and is associated with the deformation of 2×2 cells aggregates under compression. For some particular directions of loading on cellular materials with a regular structure (which carry axial or membrane load), the above bifurcation is the only deformation mechanism determining the critical load (e.g., the transverse uniaxial compression in the X -direction [9]) and a long-wave mode does not exist.

The above conclusions have been made when the response of honeycombs with straight (plate) walls and lattice structure, which deform by buckling, were examined. Analytical studies have been carried out to identify localisations due to the ‘long wave’ deformation modes under quasi-static uniaxial compression as well as under biaxial compression on assumed infinite blocks [7]. The existence of a long-wave deformation mode, which depends on the number of cells and direction of loading, is the cause of producing various patterns of

strain localization in hexagonal honeycombs. Long-wave buckling modes were also observed in square honeycombs under biaxial compression [8].

Recently, full-scale numerical simulations have attracted considerable research interest due to the localization of deformation [10-13]. Numerical studies were carried out to identify strain localization under uniaxial compression mainly due to defects [13] or caused by the structural topology [11] or dynamic effects [10,12].

The deformation mechanism of circular honeycombs, however, is different from buckling and it is difficult to describe analytically so that little is reported in the literature regarding the deformation of circular honeycombs. Moreover, the cells within a block of honeycomb experience different local strains under compression depending on the direction of loading. Numerical simulations were carried out to obtain the critical biaxial stress in honeycombs made of a visco-elastic material depending on the direction of loading [3,5] while a structural approach was employed to obtain the characteristic stresses of circular honeycombs made of perfectly plastic material [14]. To our knowledge, no theoretical studies have been published to analyze the deformation and strain localization in this material under biaxial compression.

The present study is restricted to the analysis of an in-plane biaxial compression of circular honeycombs performed with the biaxial loading device designed and installed in the Hong Kong University of Science and Technology when considering a quasi-static and low velocity impact loading. The description of this device is presented in [15]. The strain localisation is the focus of the analysis when using a structural approach. The deformation mechanism, which is based on the deformation of elastic rings within representative blocks, is analysed when using the concept of a representative block. It is not possible to define a long-wave deformation mode in circular honeycombs, so that the strain localization as observed from the experiments is analysed from the phenomenological viewpoint. The strain localisation is studied when considering a finite block under an equi-biaxial displacement-controlled loading. The velocity field along the boundary is prescribed by assuming a Coulomb friction existed on the interface between the loading device and the honeycomb specimen. A comparison between the analytical model and quasi-static test results is presented.

2 Solution methodology

A finite block of circular honeycombs is subjected to a prescribed velocity field at the boundaries. The applied velocities are defined in a way to represent the loading conditions of experimental device used in the bi-axial tests. The phenomenological approach, which is adopted in our analysis on the strain localization in a honeycomb material, is based on the upper bound theorem with respect to the power balance. The latter is used to obtain the remote biaxial stresses applied to a 2×2 cells block and to a finite honeycomb block.

The deformation energy inside the finite block is determined for kinematically admissible deformation modes, which can develop under bi-axial loading. These modes are defined with rectangular boundaries, so they are used to model the deformation of a finite honeycomb block. Due to the geometric constraints for some deformation modes, not all remote strains defined for the 2×2 cells blocks are admissible, so that an optimization of the boundaries of these blocks inside the deformed finite block is carried out to minimise the error in satisfying the geometric constraints. The remote stresses for the finite block are obtained assuming a non-uniform strain field inside the finite block and a possible uniform field in order to analyse the effect of the strain localisation.

The typical deformation modes are identified from the experimental observations and described analytically. It is shown that the selected 2×2 cells block can be used to model homogeneous deformation patterns when using a single deformation mode for an infinite block of circular honeycombs. The stress-strain characteristics of the deformation modes are analysed and the maximum bending strains for each mode are calculated in order to estimate the accuracy and the validity of the proposed model.

The following simplifying assumptions are used in the analysis:

(i) The cell wall material is approximated as a non-linear elastic material but no viscous effects are taken into account. The solution methodology assumes continuous compression of the 2×2 cells blocks when no unloading across the cell wall occurs. Therefore, the material loading path follows the analytical stress-strain curve for a continuous loading. No residual strain in the cells is taken into account.

(ii) It is assumed that the velocities at the interface between the loading device and the honeycomb block are characterised by two components in order to represent the loading conditions for the specific loading device. The velocity component, which is perpendicular to the boundary of the material block, is uniform and equal to the velocity of the loading device,

while the other velocity component, which is tangential to the boundary of the material block, is non-uniform due to the existence of friction.

(iii) The finite block under study is divided into rectangular blocks of 2×2 cells whilst each of these small blocks is characterised by their in-plane strains in the X - and Y - directions. Consequently, the strain field in the finite block is considered as a piecewise constant.

3 Deformation modes

3.1 Experimental observations

The honeycomb used in the experiments had circular cells in a hexagonal close packed arrangement (Fig. 1(a)) and it is made from polycarbonate extruded tubes with radius, $R = 3.4$ mm and an average wall thickness $t = 0.151$ mm forming a block with a depth of 2.54mm. The density of the polycarbonate is $\rho = 1191$ kg/m³.

The loading device manufactured at HKUST and used for biaxial compression is shown in Fig. 1(a). The four arms have equal lengths, $L_X = L_Y = L$. Two lower arms remained stationary while the upper two arms, which were rigidly connected, could move downwards to compress the honeycombs. One can see that the resulting loading is a special case of biaxial loading when equal remote in-plane strains are assigned to the honeycomb block since the displacements in both in-plane directions are equal. Nevertheless, the deformation inside the block was not homogeneous and different patterns of the cells deformation could be distinguished. The cells attached to or close to the corners where the stationary and the moving arms meet in the loading device experienced larger deformation in comparison to the cells, which are close to the other two corners, as shown in Fig. 1(b).

From the experimental results on quasi-static in-plane compression, several different deformation modes can be identified and they are shown in Fig. 2 (a-d); the names C_x , Sh , F and C_y , respectively are used in the further analysis. Note that modes C_x and Sh develop at relatively small displacements of the moving arms of the loading device while mode F is observed at relatively large displacements. Mode C_y is observed initially at the places with strain localizations while it occurs in a larger area inside the tested honeycomb block when the remote displacements increase.

It is known that different directions of loading on materials with periodic structure initiate and eventually support different stress-strain fields, which allow for different arrangements of the cells into characteristic repetitive groups [2,3,16]. Characteristic deformation modes, which develop for a particular direction of loading, are more clearly observed for uniaxial compression while a mixture of different deformation modes appears in the experiments under

an in-plane biaxial loading, particularly when a finite block of honeycombs is considered [2]. Presumably, different compressive strains, ε_x and ε_y , occur locally and the local ratio $\varepsilon_x/\varepsilon_y$ determines the observed mode types.

3.2 Description of the deformation modes

To simplify the analytical description of the deformation of circular honeycombs, it is assumed that only a point connection exists between neighbouring circular cells, although finite bonding is a characteristic of the actual material. The evolution of a circular ring into an ellipse is the only geometric transformation used to describe the deformations in a honeycomb material with circular cells. It is assumed that the cells are not extensible and therefore the perimeter of the cells remains constant while the ellipse curvature varies continuously during deformation. With respect to the ellipse perimeter,

$$p_{el} \approx 2\pi\sqrt{(a^2 + b^2)}/2 = 2\pi R \quad (1)$$

($2a$ and $2b$ are the major and minor axis of the ellipse, respectively) under some simplifying conditions, the variation of $2a$ can serve as a single variable to describe the evolution of the cell shapes within the representative block with a sufficient accuracy. It should be noted that the condition of the constant arc lengths between the connecting points of the cells cannot be expressed analytically but can be obtained by an iteration procedure.

The deformation patterns are found in an *ad hoc* manner from the experimental results. The characteristic deformation modes are defined assuming an infinite block of honeycombs when considering representative blocks of 2×2 cells and assuming periodicity conditions at the rectangular boundaries of the block (see Figs. A1(a,b) and A2(a,b) in the Appendix).

Modes with equal strains in the X - and Y - directions can exist under equi-biaxial compression. One such mode is the F mode (Fig. 3(a)), which is characterized by one undeformed cell surrounded by six deformed cells. This mode has been defined also for hexagonal honeycombs [16,17]. In a way of contrast with the hexagonal honeycombs, Sh mode in circular honeycombs (Fig. 3(b)) is also characterized by $\varepsilon_x = \varepsilon_y$ but consists of equally deformed cells, whose deformation can be described as ‘rotation’ of the cells against each other along with compression. The variation of the major semi-axis, $a(\delta_x)$, of the characteristic cells of modes Sh and F is obtained numerically when satisfying the condition of equal arc length between the cell connections.

Under a stress controlled loading, deformation modes having different strains in the X - and Y - direction can form (Fig. 3(c,d)). Mode Cx is characterized by $\varepsilon_x > \varepsilon_y$ while $\varepsilon_x < \varepsilon_y$ is the

characteristic of mode Cy . These modes consist of two equally deformed cells (marked as 3) and two others (marked as 1 and 2) with deformations different from the previous ones and also between themselves. This feature is a specific characteristic of the circular honeycombs and is not observed in hexagonal honeycombs (at least has not been reported as a particular feature). It should be noted that Mode $Cy1$ and $Cy2$ can be described as mode Cx , which has been rotated at angle $-\pi/3$ or $\pi/3$ with respect to the X - axis as shown in Fig. 3(d). Note that for equal remote strains ε_x and ε_y , the cells, which form modes Cx and Cy , experience different bending deformations due to the different characteristic remote displacements δ_x and δ_y . The geometric relationships for the deformation modes are presented in the Appendix.

It should be noted that in order to satisfy the condition of equal arc lengths between the connecting points, a certain relationship between the displacements in the x - and y -directions for Cx and Cy modes must be satisfied when referred to the local coordinate system (x', y') . The displacement constraint, as a ratio between the displacements $\delta_{x'}$ and $\delta_{y'}$, has been obtained numerically and approximated by two polynomial functions using a standard curve-fit procedure as

$$\frac{\delta_{x'}}{\delta_{y'}} = \begin{cases} s_0 + \sum_{k=1}^4 s_k (\bar{\delta}_{x'})^k, & \delta_{x'} \leq 0.08R \\ q_0 + \sum_{k=1}^4 q_k (\bar{\delta}_{x'})^k, & \delta_{x'} > 0.08R \end{cases}, \quad \bar{\delta}_{x'} = \delta_{x'}/2R. \quad (2a,b)$$

The local coordinate system of mode Cx coincides with the global coordinate system (X, Y) , while rotation at $\pm \pi/3$ applies to obtain mode Cy . The polynomial coefficients, s_k and q_k , $k = 0, \dots, 4$, in Eq. (2) are given in the Appendix (Table 1). As a result, the variations of the three characteristic axes, $2a_i$, ($i = 1, 2, 3$) of the cells of modes Cx and Cy are not independent. The variations of the major semi-axis, a_i , of each circular cell are different and can be approximated as

$$a_i/R = p_{0i} + \sum_{k=1}^4 p_{i,k} (\bar{\delta}_{x'})^k, \quad \bar{\delta}_{x'} = \delta_{x'}/2R \quad (3)$$

where the polynomial coefficients are given in the Appendix (Table 2). (See also Fig. A2(d), which shows the variation of the three axes).

3.3 Comparative properties of the deformation modes

The stress-strain dependence for the actual non-linear elastic material (polycarbonate) and its approximation used in the calculations are presented in Fig. 4 where the initial elastic

modulus, $E = 1.14$ GPa is also shown. Due to the different deformation of the cells within each representative block, equal remote compression strains cause different bending strains of the cells. The simplified expression for the perimeter of the ellipse dictates that the analytical model is accurate for the variations of the ellipse axes up to $a = 1.31R$, $b = 0.54R$. For these particular values, the maximum bending strain in a cell is marked as 1 in Fig. 4(a). The maximum bending strains for the modes F and Sh associated with the largest curvature of the ellipse are shown in Fig 4(a) for equal remote strains, $\varepsilon_x = \varepsilon_y = 0.1$ and are denoted as 2 and 3, respectively. It is evident, that for the same remote compressive strains, larger bending strains develop in the cells of the F mode. The maximum strains in the cells of modes Cx and Cy have three different values, which are shown in Fig. 4(b) and (c). A careful comparison between the last two figures shows that larger strains develop in mode Cy , particularly in the most deformed cell marked as 1.

Characteristic deformation modes depending on the direction of loading have been defined for hexagonal honeycombs [1,16]. Since the same hexagonal arrangement exists in the honeycomb with circular cells, it is worth comparing the deformation modes in both honeycomb materials. From geometric viewpoint, similarities exist between the deformation modes in hexagonal and circular honeycombs due to the similar specific structural symmetry in both materials as shown in Fig. 5. One can see that the F mode develops in both materials for equi-biaxial compression under a strain controlled loading. Mode Cx ($\varepsilon_x > \varepsilon_y$) in the circular honeycomb is similar to the corresponding mode in hexagonal honeycomb [16,17]. On the other hand, significant differences between the deformation modes in the two materials exist. An equal strain mode, Sh , exists in the circular honeycomb while there is no corresponding mode in the hexagonal honeycomb. The deformation modes with $\varepsilon_x < \varepsilon_y$ in both materials are different. Equally deformed cells characterise the deformation mode, which has larger ε_y strain in hexagonal honeycombs and this mode is quite similar to the deformation mode developed due to a uniaxial compression in the Y - direction. Mode Cy ($\varepsilon_x < \varepsilon_y$) comprises non-equally deformed cells in the circular honeycomb and it has no similarity with the compression mode in the Y - direction.

It should be noted that the deformation modes in elastic circular honeycombs can ‘transform’ during a continuous biaxial compression due to the ‘rotation’ of the cells and the global deformation pattern in a particular direction can consist of modes characterised by $\varepsilon_x > \varepsilon_y$, $\varepsilon_x = \varepsilon_y$ and $\varepsilon_x < \varepsilon_y$ (Fig. 6).

4 Stress-strain relationships for the different deformation modes

The remote stresses for the 2×2 cells block are obtained in order to select the deformation modes, which can appear under a bi-axial compression. If two modes are defined for the same remote strain, then the one, which possesses a lower stress, is selected to participate in the deformation pattern of a finite block.

The definition for the stresses and strains in a honeycomb is based on the response of representative blocks for each deformation mode in biaxial compression. According to the upper bound theorem, the power balance can be expressed as

$$\dot{W} = \dot{U}_{el}, \quad (4)$$

where U_{el} is the deformation energy per unit depth of the 2×2 cells block. The external power per unit depth of the block is

$$\dot{W} = F_x \dot{\delta}_x + F_y \dot{\delta}_y = d_x d_y (\sigma_x \dot{\epsilon}_x + \sigma_y \dot{\epsilon}_y) \quad (5)$$

where $d_x = 4R$ and $d_y = 2R\sqrt{3}$ are the initial dimensions of the representative block and the dot denotes differentiation with respect to time. The stresses and strains are defined per unit depth of the honeycomb as

$$\sigma_x = F_x / d_y, \quad \sigma_y = F_y / d_x, \quad (6)$$

$$\epsilon_x = \delta_x / d_x, \quad \epsilon_y = \delta_y / d_y, \quad (7)$$

where F_x and F_y are the remote force components while δ_x and δ_y denote the displacements in the X - and Y -directions, respectively. The deformation energy per unit depth of the block is expressed as

$$U_{el} = \sum_{i=1}^4 \left\{ \frac{R}{2} \int_0^{2\pi} \left[2 \left(\frac{1}{R} - \frac{1}{r_{el}(\theta)} \right)^2 \int_0^{t/2} E(\theta, z) z^2 dz \right] d\theta \right\}_i \quad (8)$$

where the coordinate z is through the wall thickness and $1/r_{el}(\theta)$ is the current curvature of each ellipse ($i = 1, \dots, 4$) forming the 2×2 cells block. The maximum bending strain is defined at $z = t/2$ as

$$\epsilon(r_{el}, t/2) = \frac{t}{2R} \left(1 - \frac{R}{r_{el}} \right) \quad (9)$$

for the current curvature of the ellipse, $1/r_{el}$.

The formulation of strain controlled loading is used for the modes Sh and F characterised by $\epsilon_y = \epsilon_x$ and the stress is obtained as

$$\sigma_x + \sigma_y = \frac{1}{d_x d_y} \frac{dU_{el}(\delta_x, \delta_y)}{d\epsilon_x}. \quad (10)$$

The characteristic strains ϵ_x , ϵ_y of modes Cx and Cy are related through the ratio between the admissible displacements $\delta_{x'}$ and $\delta_{y'}$, so that the stresses associated with these modes can be expressed as

$$\sigma_x + \gamma\sigma_y = \frac{1}{d_x d_y} \frac{dU_{el}(\delta_x, \delta_y)}{d\epsilon_x} \quad (11)$$

when using Eqs (4) – (7) together with Eq. (2). In Eq. (11), $\gamma = 2\delta_{y'}/\delta_{x'}\sqrt{3}$, $0 < \gamma < 1$ for mode Cx and $\gamma = 2\delta_{x'}/\delta_{y'}\sqrt{3}$, $\gamma > 4/3$ for mode Cy . Eqs (10) and (11) do not take into account the reduction of the initial size, $d_x \times d_y$, of the representative block during deformation.

The characteristic stresses for the analysed deformation modes are shown in Fig. 7. It appears that the F mode defined for the circular honeycombs has higher deformation energy and higher stress, respectively, than mode Sh , which explains why F mode does never develop for small strains in circular honeycombs. It is observed from the experiments that a well developed F mode (such as the one shown in Fig. 2(c)) occurs inside the finite block for relatively large remote strains when the initially formed Sh or Cy mode transform into a F -like mode. The hugely deformed surrounding cells cause an unloading of the central cell, which becomes a circle again. However, the proposed analytical model of deformation is not capable of describing these large deformations. In the further analysis of strain localization the F mode is excluded and only modes Sh , Cx and Cy are used.

5 Strain localisation – phenomenological approach

The strain inhomogeneity within a finite block is modelled by assuming that the 2×2 cells blocks forming the large block of honeycombs have a piecewise constant strains, which can be accommodated by the different deformation modes. This assumption leads to a model, where the 2D blocks remain rectangular and no shear occurs at the boundaries of the 2×2 cells blocks. All previously described biaxial modes have ε_x and ε_y components, which vary during the deformation process, so that they are capable of describing an inhomogeneous compression in the manner shown in Fig. 8. If the deformation in the X -direction is considered within a finite block of honeycomb under biaxial compression, a possible scenario of inhomogeneous compression could be the one shown in Fig. 8(a). The nearest 2×2 block experiences large deformation in the X -direction having $\varepsilon_x > \varepsilon_y$, which could gradually decrease transforming into the strain state $\varepsilon_x = \varepsilon_y$ and eventually forming further a field with $\varepsilon_x < \varepsilon_y$. The total compression in the X -direction is equal to the sum of the compression of each 2×2 blocks, when each of these blocks has a particular ε_y defined for the corresponding mode. Similar situation can be described when analysing compression, which develops in the Y -direction as shown in Fig. 8(b). In this case, the total compression in the Y -direction is equal to the sum of the compression of each 2×2 blocks, when each of these blocks has a particular ε_x defined for the corresponding mode. A combination of such ‘rows’ and ‘columns’ within a finite block of honeycombs can model an inhomogeneous biaxial compression.

5.1 Prescribed velocity field at the boundaries

The proposed approach is used to analyse the strain localization when it is caused by inhomogeneous conditions at the boundaries of the finite block. For a quasi-static or low velocity compression produced by the biaxial compression device shown in Fig. 1(a), the friction between the specimen and the device arms can be a source of the observed inhomogeneous deformation of the finite block. The numerical simulations of in-plane equi-biaxial compression with different friction coefficients at the boundaries of the honeycomb block reported in [15] show that a larger friction causes a more expressed inhomogeneity of deformation insight the block.

The global coordinate system (X, Y) is shown in Fig. 1(a). The boundary conditions at the interfaces between the device and the specimen ($L_X = L_Y = L$) can be defined as particular

velocity fields with components $V_X(X,Y)$ and $V_Y(X,Y)$ at the loading interface $(X=L, Y \in [0,L])$, $(Y=L, X \in [0,L])$ and stationary interface $(X=0, Y \in [0,L])$, $(Y=0, X \in [0,L])$. Using these velocity fields, the corresponding displacements at the interfaces can be obtained for any given time, t^* as

$$\delta_X(X, L, t^*) = V_X(X, L)t^* , \quad \delta_Y(L, Y, t^*) = V_Y(L, Y)t^* . \quad (12a,b)$$

The 2×2 cell blocks at the boundaries of the finite block can be considered as ‘boundary layers’ having ‘thickness’ of $4R$ along the Y - axis and $2R\sqrt{3}$ along the X - axis and the global displacements defined by Eqs (12a,b) can be used as prescribed conditions at these ‘boundary layers’. There is no separation between the specimen and loading arms, so that their displacements at the corner $(X=L, Y=L)$ are equal, namely $\Delta_X(t^*) = \delta_X(L, L, t^*)$ and $\Delta_Y(t^*) = \delta_Y(L, L, t^*)$, where Δ_X and Δ_Y are the prescribed displacements of the loading device.

The velocity fields induced by the loading device at the boundary interfaces of the specimen are characterised by two components (V_X, V_Y) . Constant velocity is applied in the direction normal to the specimen boundaries, namely

$$V_X = V_0 \text{ at } X = L, Y \in [0, L] \quad (13a)$$

and

$$V_Y = V_0 \text{ at } Y = L, X \in [0, L] , \quad (13b)$$

while

$$V_X = 0 \text{ at } X = 0, Y \in [0, L] \quad (14a)$$

and

$$V_Y = 0 \text{ at } Y = 0, X \in [0, L] . \quad (14b)$$

For zero friction between the device and the specimen, the other two corresponding velocity components, which occur in the specimen, vary between 0 and V_0 linearly due to the material compressibility. Therefore,

$$V_Y = V_Y(Y) \text{ at } X = L, Y \in [0, L] , \quad X = 0, Y \in [0, L] \quad (15a)$$

while

$$V_X = V_X(X) \text{ at } Y = L, X \in [0, L], \quad Y = 0, X \in [0, L] . \quad (15b)$$

In this case, a uniform displacement and strain fields are determined at the specimen boundaries.

The friction opposes the relative motion of the surfaces trying to bring the two surfaces in one velocity. Therefore, it is expected that velocities components $V_X^* = V_X^*(X)$ and $V_Y^* = V_Y^*(Y)$ will deviate from linear distribution in a way that

$$V_X^* > V_X \text{ on } Y = L, X \in [0, L] \quad (16a)$$

and

$$V_X^* < V_X \text{ on } Y = 0, X \in [0, L] \quad (16b)$$

except for the points $(X=L, Y=L)$, $(X=L, Y=0)$, $(X=0, Y=0)$ and $(X=0, Y=L)$ where the velocities are fixed. The same relationship holds for velocity V_Y^* , namely

$$V_Y^* > V_Y \text{ on } X = L, Y \in [0, L] \quad (17a)$$

and

$$V_Y^* < V_Y \text{ on } X = 0, Y \in [0, L], \quad (17b)$$

where V_X and V_Y are the velocity components for zero friction.

The above velocity fields are well described by the following dependence

$$V_X^*(X) = V_0 X [1 + g(\mu)(1 - X/L)]/L, \quad V_Y = V_0 \quad (18a)$$

at the moving boundary $Y = L, X \in [0, L]$ and

$$V_Y^*(Y) = V_0 Y [1 + g(\mu)(1 - Y/L)]/L, \quad V_X = V_0 \quad (18b)$$

at the moving boundary $X = L, Y \in [0, L]$. The velocity components at the specimen interface with the stationary boundaries are

$$V_X^*(X) = V_0 X [1 - g(\mu)(1 - X/L)]/L, \quad V_Y = 0 \quad (19a)$$

at $Y = 0, X \in [0, L]$ and

$$V_Y^*(Y) = V_0 Y [1 - g(\mu)(1 - Y/L)]/L, \quad V_X = 0 \quad (19b)$$

at the boundary $X = 0, Y \in [0, L]$. In Eqs (18) and (19), $g(\mu)$ is a constant depending on the friction coefficient μ ; it is anticipated that $g(\mu)$ is larger for larger friction. The variations of the velocity components along the specimen boundaries are schematically shown in Fig. 9(a) for two values of $g(\mu)$. Larger velocity deviation from the linear dependence is described by Eqs. (18) and (19) for the larger friction. When the displacements of the moving arms are prescribed as $\Delta_X(t) = V_0 t$, the strain distribution at the moving boundary at any $t = t^*$ is defined as

$$\varepsilon_x(X, L, t^*) = \frac{d(\delta_x)}{dX} = \frac{\Delta_X(t^*)}{L} [1 + g(\mu)(1 - 2X/L)], \quad (20a)$$

at $Y = L, X \in [0, L]$ and

$$\varepsilon_y(L, Y, t^*) = \frac{d(\delta_Y)}{dY} = \frac{\Delta_Y(t^*)}{L} [1 + g(\mu)(1 - 2Y/L)] \quad (20b)$$

at $X = L, Y \in [0, L]$. The strain variations along the moving and stationary boundaries are presented in Fig. 9(b) for equal average strains $\varepsilon_x = \Delta_x / L$ and $\varepsilon_y = \Delta_y / L$, which show that the prescribed boundary conditions determine increasing strain non-uniformity along both boundaries for non-zero friction. This type of deformation can be modelled by the modes C_x and C_y , respectively, which have rectangular boundaries.

5.2 Deformation of a finite block

A finite block of honeycombs consisting of 14×16 cells is modelled. This particular dimension, resulting in $L_x = 95.2$ mm and $L_y = 94.22$ mm, is selected to be comparable as close as possible to the experimental setup of a 100 mm \times 100 mm block. It is assumed that the characteristic strains of the modes inside the block are characterized by piecewise constant values determined by the compression of the C_x , C_y or Sh modes. In order to accommodate the described inhomogeneity, ‘boundary layers’ are formed where deformation modes C_x having $\varepsilon_x > \varepsilon_y$ are placed in the X -direction along the boundary $Y = L_y, 0 < X < L_x$ but modes C_y model the non-uniform compression in the Y -direction along the boundary $X = L_x, 0 < Y < L_y$. It is assumed that $\varepsilon_x = \varepsilon_y$ for the 2×2 cells block placed at the corner ($X = L_x, Y = L_y$) according to Eq. (20), in which strain state is represented by mode Sh . When one of the in-plane strains for the particular modes participating in the ‘boundary layer’ along the moving boundaries is prescribed, the other strain is calculated according to the mode type. The strains defined by Eqs (20a,b) should be considered as prescribed boundary conditions.

The following assumptions are used to construct the displacement and strain field inside the finite block: (i) the displacements, δ_x^{ij} and δ_y^{ij} , $i = 1, \dots, 7$; $j = 1, \dots, 8$, are continuous and determine the boundaries of the 2×2 cells blocks; (ii) the strains are assumed piecewise constant and are defined as

$$\varepsilon_x^{ij} = \delta_x^{ij} / 4R, \quad \varepsilon_y^{ij} = \delta_y^{ij} / 2R\sqrt{3}, \quad i = 1, \dots, 7; j = 1, \dots, 8, \quad (21a)$$

where

$$\delta_x^{ij} = 4R - |x_{i,j} - x_{i+1,j}|, \quad \delta_y^{ij} = 2R\sqrt{3} - |y_{i,j} - y_{i,j+1}|, \quad i = 1, \dots, 7; j = 1, \dots, 8. \quad (21b)$$

It is seen from the above definitions that the deformation inside the finite block is modelled by generalized rectangular 2×2 cells blocks characterized only by compression similarly to the

‘boundary layer’. In other words, it is anticipated that a combination of modes Cx , Cy and Sh can represent the deformation of the macro block. It has been already discussed that modes Cx and Cy are only defined for those displacements δ_x^{ij} and δ_y^{ij} , which satisfy the geometric compatibility condition $\delta_x/\delta_y = f(\delta_x)$ (Eq. (2) in the corresponding local coordinate system (x', y')).

The above methodology follows somehow the classical idea that strain localization can be defined for larger honeycomb blocks [7,8] when analysing the deformation of the 2×2 cells blocks. However, due to the particular deformation of the circular honeycombs, the resulting deformation field cannot be called long-wave ‘buckling modes’. Moreover, the deformation of a cell is not due to the buckling of the ligament (‘Type II’ structure [18]) but involves ovalization of a circle (‘Type I’ structure [18]). To authors’ knowledge, no theoretical study reported in the literature has considered the mechanism of strain localization in materials with open cells and a regular structure, where the dominant deformation mechanism possesses characteristics of ‘Type I’ structures.

An example for a piecewise constant strain distribution in a finite block is considered for a biaxial deformation under remote displacement control for the case of equal remote strains $\varepsilon_x = \varepsilon_y$, where

$$\varepsilon_x = \Delta_x / L_x, \quad \varepsilon_y = \Delta_y / L_y, \quad (22a,b)$$

$\Delta_x(t)$ and $\Delta_y(t)$ are the controlled displacements in the corresponding direction. The following equalities take place for the ‘ j ’-th row and the ‘ i ’-th column in the block

$$L_x(1 - \varepsilon_x) = L_x \left(1 - \frac{1}{7} \sum_{i=1}^7 \varepsilon_x^{ij} \right), \quad L_y(1 - \varepsilon_y) = L_y \left(1 - \frac{1}{8} \sum_{j=1}^8 \varepsilon_y^{ij} \right) \quad (23a,b)$$

when satisfying Eq. (2) for modes Cx and Cy . Since the different deformation modes are defined depending on the relative strain variation, their appearance inside the finite block can be an indication for the particular dominant local strain.

According to Eqs (21a,b), the strain distribution inside the finite block is defined by the relative displacements, $(\delta_x^{ij}, \delta_y^{ij})$, of the boundaries of the 2×2 cells blocks, which are determined by the co-ordinate points $\{(x_{i,j}, y_{i,j}), (x_{i+1,j}, y_{i,j}), (x_{i+1,j}, y_{i,j+1}), (x_{i,j}, y_{i,j+1})\}$, $i = 1, \dots, 6, j = 1, \dots, 7$. These co-ordinate points are varied iteratively to obtain the admissible ratios $(\delta_x^{ij} / \delta_y^{ij})$ for any global displacement of the boundaries of the finite block δ_x, δ_y . The global displacements are increased incrementally according to Eqs (12), $t^* = t + \Delta t$. The

displacements (δ_x^j, δ_y^j) are obtained by minimization of the difference, $\bar{\Delta}$, between the displacement ratios $\left(\frac{\delta_x^j}{\delta_y^j}\right)$ obtained at the current iteration step and the analytical dependence $\left(\frac{\delta_x^j}{\delta_y^j}\right)^{an}$

$$\bar{\Delta} = \min_{\delta_x, \delta_y} \sum_{i=2}^7 \sum_{j=2}^8 \left[\left| \left(\frac{\delta_x^j}{\delta_y^j} \right) - \left(\frac{\delta_x^j}{\delta_y^j} \right)^{an} \right|_{Cx} + \left| \left(\frac{\delta_{x'}^j}{\delta_{y'}^j} \right) - \left(\frac{\delta_{x'}^j}{\delta_{y'}^j} \right)^{an} \right|_{Cy} + \left| \left(\frac{\delta_x^j}{\delta_y^j} \right) - \left(\frac{\delta_x^j}{\delta_y^j} \right)^{an} \right|_{Sh} \right] \quad (24)$$

In Eq. (24), $\left(\frac{\delta_x^j}{\delta_y^j}\right)^{an}$ and $\left(\frac{\delta_{x'}^j}{\delta_{y'}^j}\right)^{an}$ are defined by Eq. (2) for modes Cx and Cy , respectively, while $\left(\frac{\delta_x^j}{\delta_y^j}\right)^{an} = 2/\sqrt{3}$ for mode Sh .

6 Comparison with the experimental results

The variations of the ratios $\delta_{x'}/\delta_{y'}$ in the local coordinate systems of the Cx and Cy modes are shown in Fig. 10(a) for $\varepsilon_x = \varepsilon_y = 0.025$. The solid dots correspond to the Cx modes while the open symbols represent the Cy modes. It can be noticed from this figure that a large number of macro blocks are characterized by displacements approaching $\delta_{x'}/\delta_{y'} = 2/\sqrt{3}$, which characterizes the equal strain mode Sh . Therefore, it is concluded that a mixture of modes Cx , Cy and Sh can occur in the finite block under the assumed boundary conditions. Another way to measure the strain inhomogeneity is to analyze the variation of the local strain ratios $\varepsilon_x^j/\varepsilon_y^j$ or $\varepsilon_y^j/\varepsilon_x^j$. For this particular example, the largest values of these ratios are obtained as $\varepsilon_x^j/\varepsilon_y^j = 1.83$, which is characteristic of mode Cx , at the corner $X = 0, Y = L_Y$ and $\varepsilon_y^j/\varepsilon_x^j = 2.44$ characterizing mode Cy at the corner $X = L_X, Y = 0$.

The strain distributions in a finite block under the same boundary conditions but at an increased strain, $\varepsilon_x = \varepsilon_y = 0.0625$ are discussed next. Figure 10(b) shows that similar to the previous case, a mixture of modes exist in the block, however, the inhomogeneity is larger characterized by $\varepsilon_x^j/\varepsilon_y^j = 2.24$ at the corner $X = 0, Y = L_Y$ for the mode Cx , while $\varepsilon_y^j/\varepsilon_x^j = 2.86$ is obtained for strains at corner $X = L_X, Y = 0$, thus determining mode Cy . The strain distributions in the honeycomb block, shown as ratios between the local strain components and their average values, are schematically presented in Figs. 11(a) and (b). It is evident that the smallest strains are observed near to the corners $(X = L_X, Y = L_Y)$ and $(X = 0, Y = 0)$ while the largest strains are observed at the other two corners. The variation of the ratio $\varepsilon_x^j/\varepsilon_y^j$ within the finite block is shown in Fig. 11(c). A large area inside the block is characterized by strain ratios

around one and slightly smaller than one, which shows that modes Sh and Cy are developed. The largest strain localization is captured by modes Cx and Cy , near the corners with material velocity either ($V_X = 0, V_Y \neq 0$) or ($V_Y = 0, V_X \neq 0$).

The experimentally observed deformation pattern for $\varepsilon_X = \varepsilon_Y \approx 0.06$ is shown in Fig. 11(d) together with three characteristic modes obtained from the analytical model. A more visible tendency for deformation modes Sh is evident, while the strain localization occurs with the Cx and Cy modes.

According to the upper bound theorem, the power balance can be expressed as

$$\dot{W}_e = \dot{W}_i + \dot{W}_f. \quad (25)$$

The external power is

$$\dot{W}_e = F_X \dot{\Delta}_X + F_Y \dot{\Delta}_Y \quad (26)$$

which can be calculated under a strain (displacement) controlled loading, $\dot{\varepsilon}_X = \dot{\varepsilon}_Y$

$$\dot{W}_e = \dot{\varepsilon}_X H L_X L_Y (\sigma_X + \sigma_Y) \quad (27)$$

where H is the depth of the specimen. The internal power dissipated due to the deformation of the specimen is

$$\dot{W}_i = \int_{Volume} \sigma_w(\varepsilon) \dot{\varepsilon} dv, \quad (28)$$

where $\sigma_w(\varepsilon)$ is the non-linear elastic characteristic of the honeycomb wall material and ε are the bending deformations in each cell. The remote stresses are equal, $\sigma_X = \sigma_Y = \sigma$, for the loading device in Fig 1(a) so that the friction power loss is

$$\dot{W}_f = \int_{Surface} \tau_S |\Delta V_f| dS = \mu \sigma \int_{Surface} |\Delta V_f| dS, \quad (29)$$

where $|\Delta V_f|$ stands for the velocity jumps $|V_0 - V_X^*(X)|$ and $|V_0 - V_Y^*(Y)|$ along the moving boundaries and for $|V_X^*(X)|$ and $|V_Y^*(Y)|$ at the stationary boundaries. Obviously, for small friction, \dot{W}_f can be neglected in comparison with the internal energy.

The following equation can be used to obtain the remote stresses for the $L_X \times L_Y$ finite honeycomb block when assuming an equi-biaxial strain control $\dot{\varepsilon}_X = \dot{\varepsilon}_Y$

$$\sigma_X(\varepsilon_X) + \sigma_Y(\varepsilon_X) = \frac{1}{H L_X L_Y \dot{\varepsilon}_X} \int_{Volume} \sigma_w(\varepsilon) \dot{\varepsilon} dv \approx \frac{1}{H L_X L_Y \Delta \varepsilon_X} \int_{Volume} \sigma_w(\varepsilon) \Delta \varepsilon dv. \quad (30a)$$

However, the diminutions of the modelled finite honeycomb block in the X - and Y - directions differ only by 1%, so that it can be anticipated that $\sigma_X(\varepsilon_X) \approx \sigma_Y(\varepsilon_X)$, so that the expression

$$\sigma(\varepsilon_x) \approx \frac{1}{2HL_xL_y\Delta\varepsilon_x} \int_{Volume} \sigma_w(\varepsilon)\Delta\varepsilon dv \quad (30b)$$

is used to compare the experimental results with the predictions from the theoretical model.

The stress-strain variation for the analysed finite block of circular honeycombs is shown in Fig. 12 in comparison with the experimental stress-strain curve for a quasi-static loading at speed 120 mm/min. A reasonable agreement is observed, although the predicted stress is higher and the stress-strain curve diverges from the experimental test results for average strains larger than 0.15, approximately. This discrepancy is related to the accuracy of the analytical description of the deformation modes rather than to the approximation of the cell wall material. The solution methodology assumes continuous compression of the 2×2 cells blocks when no unloading across the cell wall occurs. Therefore, the material loading path follows the analytical stress-strain curve for a continuous loading when almost a constant stress is assumed for the large strains.

Due to the approximate expression for the ellipse perimeter given by Eq. (1), an increase of the large semi-axis more than $1.35R$ involves errors larger than 5% when calculating p_{el} . As it was already discussed, the cells, which form the deformation modes, experience different bending deformations (except for the mode Sh) and the largest deformations occur in one of the cells of modes Cx and Cy . For the particular example considered above, an average remote compression strain of 12% causes maximum local strains $\varepsilon_x \approx 0.25$ (with $a_1 > 1.35R$ for modes Cx and Cy) which, on the other hand, produce maximum tensile/compression strains of the cell walls of about 16%. Obviously, these large values of a_1 contribute to the poor model accuracy at increased compression. However, these characteristics are not common for the entire finite honeycomb block where many cells experience strains, which are smaller than the average ones, so that the accuracy of the model is reasonably high for these cells. The increase of the average strains causes larger strain localization, which requires larger local deformations of certain cells thereby reducing the accuracy of the model due to the assumed approximation given by Eq. (1).

A biaxial compression with equal strains can be also modelled assuming only uniform compression inside the block described by mode Sh (no friction at the boundaries exists). It is shown in Fig. 12 that the analytically obtained stress for equal strains inside the block (without localisation) is higher than the calculated stress when the strain localisation is considered. This observation implies that the inhomogeneous stress within a finite block of honeycombs occurs at lower deformation energy.

A comparison between the deformation patterns observed at a quasi-static compression at a loading speed of 120 mm/min and a low velocity impact at 4.04 m/s is shown in Fig. 13 for several compressive displacements. The impact loading was performed in Dynatup, a computerized drop weight impact test machine, which accelerated a drop weight to a specified velocity to hit the top of the bi-axial loading device shown in Fig. 1(a). It is evident that there is only a marginal difference in the observed strain localization, which cannot be attributed to dynamic effects. The density of the tested honeycomb is given by $\rho^* = (2\pi/\sqrt{3})\rho(t/2R)$ when assuming a perfect geometry, therefore $\rho^* = 96.1 \text{ kg/m}^3$. Evidently, the material density is too low in order to cause significant inertia effects at a low velocity impact, which would affect the deformation patterns in the tested honeycomb block. Similar to the quasi-static case, the strain localization is caused by the friction between the specimen and the loading device and more precisely, by the particular velocity fields at the interfaces of the device. Another design of the loading device, for example having all four arms moving, similar to the device described in [2] will cause different strain localization under equi-biaxial compression and low velocity impact.

7 Conclusions

The strain localization in a finite block of a honeycomb material under a quasi-static and low velocity impact loading is studied using a structural approach based on the deformation mechanism of circular cells made of non-linear elastic material. The deformation modes characteristic for a honeycomb material under biaxial in-plane compression are identified and described analytically for remote compression strains up to about 15%. The local strain conditions to observe these modes are determined. Some similarities with the hexagonal honeycombs under biaxial compression as well as differences between the deformation modes in the two materials are discussed. It is concluded that the particular deformation modes depend on the local strain field and modes with different dominant strains can co-exist inside a finite block subject to equi-biaxial remote strains. Using the proposed phenomenological approach to the strain localisation, it is shown that for equal remote strains, larger remote stresses would occur for the finite block when assuming homogeneous deformation in comparison to the stress when the strain inhomogeneity is taken into account. Comparison between the theoretical and experimental results is made for a quasi-static equi-biaxial compression.

Acknowledgements – The authors wish to thank Dr. L.L. Hu of the South China University of Technology (Guangzhou, China) and Dr. Z.Y. Gao of HKUST for providing their experimental results on the biaxial compression of circular honeycombs, as well as for the helpful discussions on the subject.

The financial support from the Hong Kong Research Grant Council (RGC) under grant HKUST6116/04E is gratefully acknowledged.

Accepted manuscript

References:

- [1] Gibson LJ, Ashby MF. Cellular solids: structure and properties. Oxford: Pergamon Press; 1988.
- [2] Papka SD, Kyriakides S. Biaxial crushing of honeycombs—Part I: experiments. *Int. J. Solids Struct.* 1999;36: 4367–996.
- [3] Papka SD, Kyriakides S. Biaxial crushing of honeycombs—Part II: analysis. *Int. J. Solids Struct.* 1999;36: 4397–423.
- [4] Chung J, Waas AM. Compressive response of circular cell polycarbonate honeycombs under in-plane bi-axial static and dynamic loading. Part I: Experiments. *Int. J. Impact Eng.* 2002;27: 729–754.
- [5] Chung J, Waas AM. Compressive response of circular cell polycarbonate honeycombs under in-plane bi-axial static and dynamic loading—Part II: simulations. *Int. J. Impact Eng.* 2002;27: 1015–47.
- [6] Chung J, Waas AM. In-plane biaxial crush response of polycarbonate honeycombs. *J. Eng. Mech.* 2001;127: 180–93.
- [7] Okumura D, Ohno N, Noguchi H. Post-buckling analysis of elastic honeycombs subject to in-plane biaxial compression. *Int. J. Solids Struct.* 2002;39: 3487–3503.
- [8] Ohno N, Okumura D, Niikawa T. Long-wave buckling of elastic square honeycombs subject to in-plane biaxial compression. *Int. J. Mech. Sci.* 2004;46: 1697–1713.
- [9] Gong L, Kyriakides S. Compressive response of open cell foams Part II: Initiation and evolution of crushing. *Int. J. Solids Struct.* 2005; 42: 1381–1399.
- [10] Ruan D, Lu G, Wang B, Yu TX. In-plane dynamic crushing of honeycombs—a finite element study. *Int J Impact Eng.* 2003;28: 161–82.
- [11] Zheng Z, Yu J, Li J. Dynamic crushing of 2D cellular structures: A finite element study. *Int. J. Impact Eng.* 2005; 32: 650–664.
- [12] Tan PJ, Reid SR, Harrigan JJ, Zou Z, Li S. Dynamic compressive strength properties of aluminium foams. Part II—‘shock’ theory and comparison with experimental data and numerical models. *J. Mech. Phys. Solids.* 2005;53: 2206–2230.
- [13] Guo XE, Gibson LJ. Behavior of intact and damaged honeycombs: a finite element study. *Int. J. Mech Sci.* 1999;41: 85–105.
- [14] Karagiozova D, Yu TX. Post-collapse characteristics of ductile circular honeycombs under in-plane compression. *Int. J. Mech. Sci.* 2005;47: 570–602.
- [15] Hu LL, Yu TX, Gao ZY, Huang XQ. Inhomogeneous deformation of polycarbonate circular honeycombs under in-plane compression, *Int. J. Mech. Sci.* 2007; Submitted.
- [16] Ohno N, Okumura D, Noguchi H. Microscopic symmetric bifurcation condition of cellular solids based on homogenization theory. *J. Mech. Phys. Solids.* 2002;50: 1125–53.
- [17] Saiki I, Ikeda K, Murota K. Flower patterns appearing on a honeycomb structure and their bifurcation mechanism. *Int. J Bifurcation and Chaos*, 2005;15: 497–515.[18] Calladine CR, English RW. Strain-rate and inertia effects in the collapse of two types of energy absorbing structure. *Int. J. Mech. Sci.* 1984;26: 689–701.

Figure captions

- Figure 1 Experimental setup for in-plane biaxial compression. (a) Initial arrangement and the specimen orientation; (b) A deformed stage; (c) The finite connections between the cells in the honeycomb material; (d) A typical nominal stress-strain curve for an equi-biaxial stress loading at 120 mm/min.
- Figure 2 Deformation modes from the experimental tests. (a-d) Modes Cx , Sh , F and Cy , respectively.
- Figure 3 Analytically described deformation modes. (a) Equal strain modes – F , (a) and Sh , (b); Non-equal strain modes – Cx , (c) and Cy , (d) ($Cy1$ and $Cy2$, respectively).
- Figure 4 A nominal tensile stress-strain curve for the polycarbonate material and the material approximation; Maximum bending strains in the cells of the deformation modes at $z = \pm t/2$. (a) 1 – maximum strain for the model, 2 – mode F : $\varepsilon_x = \varepsilon_y = 0.1$, 3 – mode Sh : $\varepsilon_x = \varepsilon_y = 0.1$; (b) Mode Cx : $(\varepsilon_x + \varepsilon_y)/2 = 0.079$, $\varepsilon_x = 0.108$, $\varepsilon_y = 0.0505$, 1, 2, 3 – bending strains in cells 1, 2, and 3, respectively; (c) Mode Cx : $(\varepsilon_x + \varepsilon_y)/2 = 0.079$, $\varepsilon_y = 0.116$, $\varepsilon_x = 0.042$.
- Figure 5 Comparison between the deformation modes developed under in-plane biaxial compression in materials with regular circular honeycombs, (a) and regular hexagonal honeycombs [16], (b).
- Figure 6 ‘Transformation’ of the deformation modes.
- Figure 7 Stress-strain histories for the deformation modes. (a) Equal strains modes; (b) $(\sigma_x + \sigma_y)$ refers to mode Sh , Eq. (10) and $(\sigma_x + \gamma\sigma_y)$ refers to modes Cx , Cy , Eq. (11).
- Figure 8 Possible mode evolutions during deformation in presence of strain localization to accommodate biaxial compression. (a) Deformation in the X -direction; (b) Deformation in the Y -direction.
- Figure 9 (a) Velocity components at the boundaries of the finite block of honeycombs, $g_1(\mu) < g_2(\mu)$; (b) Ratio between the compressive strains and the average strains along the boundaries.
- Figure 10 Results from the minimization procedure for the mode arrangement inside the finite block, $g = 0.1$ (The solid dots correspond to the Cx modes, the open symbols represent the Cy modes). (a) $\varepsilon_x = \varepsilon_y = 0.025$; (b) $\varepsilon_x = \varepsilon_y = 0.0625$.
- Figure 11 Strain non-uniformity in the finite block for $\varepsilon_x = \varepsilon_y = 0.0625$, $g = 0.1$ calculated according to Eq. 21(a). (a) $\varepsilon_x^{ij} / \varepsilon_x$; (b) $\varepsilon_y^{ij} / \varepsilon_y$; (c) $\varepsilon_x^{ij} / \varepsilon_y^{ij}$; (d) Experimentally observed deformation for $\varepsilon_x = \varepsilon_y \approx 0.06$.
- Figure 12 Comparison between the model predictions ($g = 0.1$) and the experimental results for biaxial in-plane compression at 120 mm/min.
- Figure 13 Comparison between the strain localisation patterns for a quasi-static compression and a low velocity impact. (a-c) Compression at 120 mm/min, (a) $\Delta_x = \Delta_y \approx 6$ mm, (b) $\Delta_x = \Delta_y \approx 9$ mm, (c) $\Delta_x = \Delta_y \approx 15$ mm; (d-f) Impact with $V_0 = 4.04$ m/s, (d) $\Delta_x = \Delta_y = 5.1$ mm, (e) $\Delta_x = \Delta_y = 9.24$ mm, (f) $\Delta_x = \Delta_y = 15.27$ mm.
- Figure A1 Geometry of the equal strain modes. (a) Mode F ; (b) Mode Sh .
- Figure A2 Modes with different remote strains. (a) Modes Cx ; (b) Mode Cy ; (c) Relationship between the remote displacements $\delta_{x'}$ and $\delta_{y'}$ for modes Cx and Cy in local coordinate system (x', y') ; (d) Variation of the major semi-axes, a_i , $i = 1, 2, 3$ of the ellipses representing the characteristic cells of modes Cx and Cy .

Figure A3 Repeatability of the representative block for the characteristic modes. (a) Mode F ; (b) Mode Sh ; (c) Mode Cx ; (d) Mode Cy .

Accepted manuscript

Table 1 Coefficients for the approximation of the displacement ratio, $\delta_{x'} / \delta_{y'}$, for modes Cx and Cy , Eq. (A6)

s_0	s_1	s_2	s_3	s_4
1.1524	-7.412	417.27	-2315.657	-1847.83
q_0	q_1	q_2	q_3	q_4
-1.4357	94.606	-938.454	4220.27	-7021.97

Accepted manuscript

Table 2 Coefficients for the approximation of the semi-axes of the ellipses describing modes C_x and C_y , Eq. (A7)

	$p_{i,0}$	$p_{i,1}$	$p_{i,2}$	$p_{i,3}$	$p_{i,4}$
a_1	1.0665	3.2956	-30.4256	165.9847	-339.3664
a_2	1.0678	3.19078	-35.74	204.735	-426.989
a_3	1.0268	2.2699	-23.922	133.348	-274.898

Accepted manuscript

Appendix: Geometric characteristics of the deformation modes

1 Modes with equal remote strains

1.1 F – mode

A block of 2×2 cells is selected to accommodate the deformation patterns, which can occur under a displacement-controlled compression. In the particular case the equal strain is $\varepsilon_x = \varepsilon_y = \varepsilon = \delta / (R\sqrt{3})$, where δ is the displacement in the Y -direction as shown in Fig. A1(a). It is assumed that the central cell remains undeformed, has no translation motion in the x - y plane but rotates clockwise at angle α . The particular value of α can be obtained when satisfying the tangential condition between the circle (centre O) and the ellipse (centre A) at point B. However, this procedure involves highly non-linear relationships between the characteristics of the deformed ellipse (the ratio b/a and rotational angles θ and ξ), so that it is anticipated that during deformation of the cells surrounding the central one the distance $\overline{AB} = R$, therefore

$$\alpha = a \cos\left(1 - \delta / R\sqrt{3}\right). \quad (\text{A1})$$

The positions of the points B and E determine angles θ and ξ , which define the rotation of the ellipse and the ratio b/a . During deformation

$$\overline{AE} + \overline{EO_1} = 2\left(R - \delta / \sqrt{3}\right) \quad (\text{A2})$$

where

$$\overline{AE}^2 = \frac{a(2R^2 - a^2)}{(2R^2 - a^2)\cos^2 \xi + a^2 \sin^2 \xi}, \quad (\text{A3})$$

$$\overline{EO_1}^2 = \frac{a(2R^2 - a^2)}{(2R^2 - a^2)\cos^2(2\pi/3 - \alpha - \theta) + a^2 \sin^2(2\pi/3 - \alpha - \theta)}, \quad (\text{A4})$$

$$\theta = 0.5a \cos\left[\frac{1 - (2 - a^2)a^2}{(a^2 - 1)}\right] \quad (\text{A5})$$

satisfy the ellipse equation.

The deformation of the model representing the F - mode is ruled by the rotation of the central cell while the bifurcation occurs with 45° with respect to the horizontal axis (see the ellipse with centre at A). This angle varies only slightly in the local coordinate system under increased compression, e.g., the large axis is inclined at about 50° at $\alpha = 30^\circ$, $\delta = 0.25R$.

1.2 *Sh* – mode

This mode is constructed in a way that the centres of the cells are aligned in both in-plane directions but all cells compress and ‘rotate’ in order to accommodate the biaxial compression as shown in Fig. A1(b). All cells comprising this mode deform identically and experience equal bending deformations. The connection point C moves along the line AD connecting the centres of the neighbouring cells while satisfying the condition for equal arc lengths $\widehat{CS} = \widehat{SE} = \widehat{EC}' = p_{el}/6$. Point S is a common point for the ellipses with centres A and B, at which these ellipses have a common tangent. The equi-biaxial strain compression is described by the variations of the ratio b/a and angles Φ_A, Φ_B , which are defined for the two characteristic cells of mode *Sh* as angles between the large ellipse axis and the x -axis of the model. These angles characterise the ‘rotation’ of the neighbouring cells in opposite directions.

2 Modes with different remote strains – mode *Cx* and mode *Cy*

These modes can develop in a way that $\varepsilon_x > \varepsilon_y$ for mode *Cx* and $\varepsilon_x < \varepsilon_y$ for mode *Cy* only when the cells deform by different amounts as shown in Figs A2(a) and (b). The largest bending deformations occur in the cells, which experience only compression in the x -direction (Fig. A2(a)) while the smallest bending deformations occur in the cells, which experience bi-axial compression. Angle Φ_3 characterises the ‘rotation’ of the latter cells. The condition for equal arc lengths, $\widehat{A_1A_2} = \widehat{A_2A_3} = \widehat{A_3A_1} = p_{el}/6$ between the connecting points (Fig. A2(a)) can be satisfied only for certain ratios of the displacements δ_x and δ_y . The following relationship must hold in the local coordinate system (x', y') of the modes

$$\frac{\delta_{x'}}{\delta_{y'}} = \begin{cases} s_0 + \sum_{k=1}^4 s_k (\overline{\delta_{x'}})^k, & \delta_{x'} \leq 0.08R \\ q_0 + \sum_{k=1}^4 q_k (\overline{\delta_{x'}})^k, & \delta_{x'} > 0.08R \end{cases}, \quad \overline{\delta_{x'}} = \delta_{x'}/2R \quad (\text{A6})$$

where the polynomial coefficients s_k and q_k are given in Table 1. The relationship $\delta_{x'}/\delta_{y'}$ is shown in Fig. A2(c); it must hold regardless the angle of rotation of the mode. Therefore, prescribing the displacement in one direction, the displacement in the perpendicular direction can be calculated accordingly. This means that the linear distribution (and any other distribution) of the displacements in one direction allows also combination of modes as long as the above geometric relationship is satisfied. The above constraint (Eq.(A6)) determines the variations of the ellipses’ characteristics, which can be approximated by polynomial functions

$$a_i/R = p_{0i} + \sum_{k=1}^4 p_{i,k} (\bar{\delta}_{x'})^k, \quad \bar{\delta}_{x'} = \delta_{x'}/2R. \quad (\text{A7})$$

The values of the polynomial coefficients $p_{i,k}$, $i = 1,2,3$; $k = 0,\dots,4$ are listed in the Table 2. The variations of the dimensionless semi-axes of the three ellipses characterising modes Cx and Cy are shown in Fig. A2(d).

3 Repeatability of the representative block for the characteristic modes

The analysed deformation modes, which can exist in an infinite block of circular honeycombs under bi-axial in-plane compression, are defined for rectangular representative 2×2 cells blocks in global co-ordinate system (X,Y) . The rectangular boundaries of each mode are shown in Figs A3(a) – A3(d). Constraints are imposed on the model in order to resemble the periodic conditions in a honeycomb material. These constraints require certain relationships between the displacement components u_x and u_y of the points marked at the boundaries of the rectangular 2×2 cells blocks. Assume that the centre of the coordinate system is placed at the centre of the bounding rectangle of each mode as shown in Figs A3(a) – A3(d). Then, the displacements, u_x and u_y , at the points, i, i' marked on the vertical boundaries are constrained to

$$u_x(i) = -u_x(i') \text{ and } u_y(i) = u_y(i'), \quad (\text{A8a,b})$$

$i = 1,2,3$ for mode F (Fig. A3(a)), $i = 1,\dots,4$ for mode Sh (Fig. A3(b)), $i = 1,2$ for mode Cx (Fig. A3(c)) and $i = 1,2,3$ for mode Cy (Fig. A3(d)). The displacements, u_x and u_y , at the points, i, i' , at the horizontal boundaries satisfy

$$u_x(i) = u_x(i') \text{ and } u_y(i) = -u_y(i'), \quad (\text{A9a,b})$$

$i = 4,\dots,7$ for mode F , $i = 5,\dots,8$ for mode Sh , $i = 3,\dots,6$ for mode Cx and $i = 4,5,6$ for mode Cy (see Fig. A3).

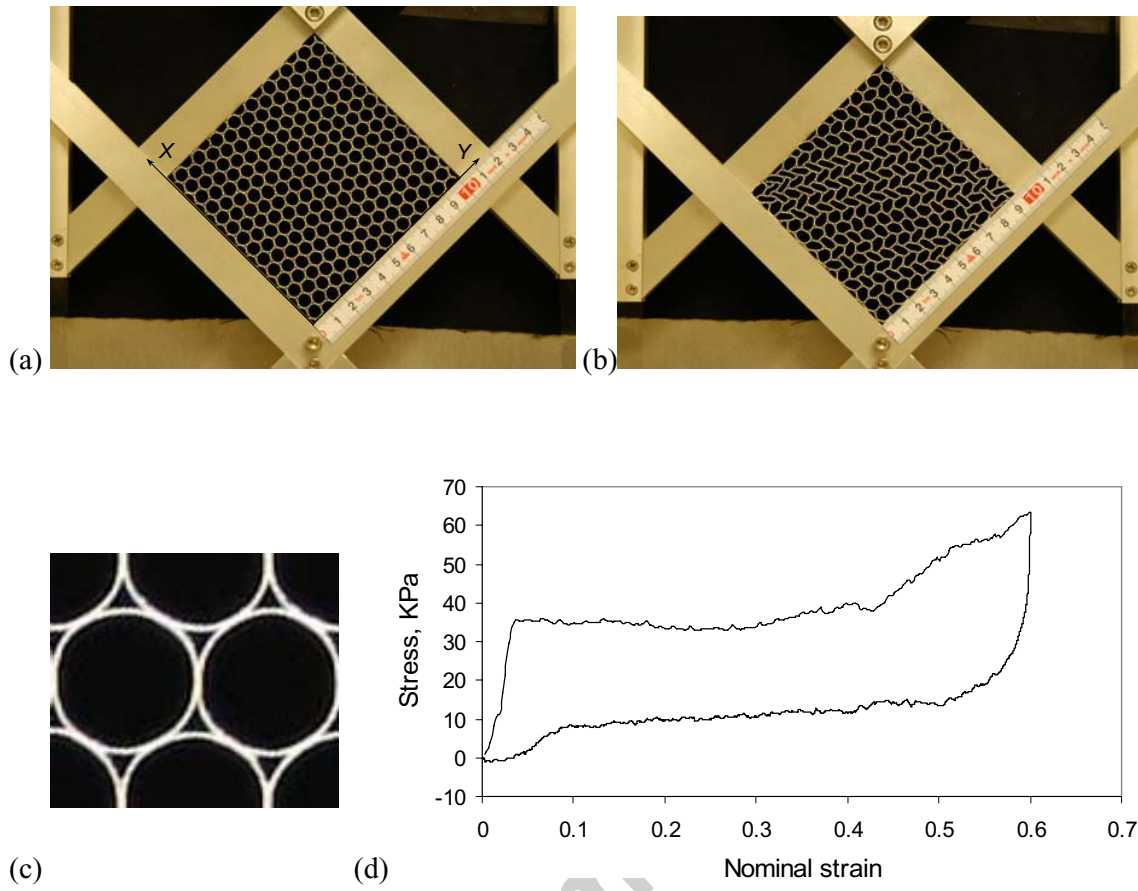


Figure 1

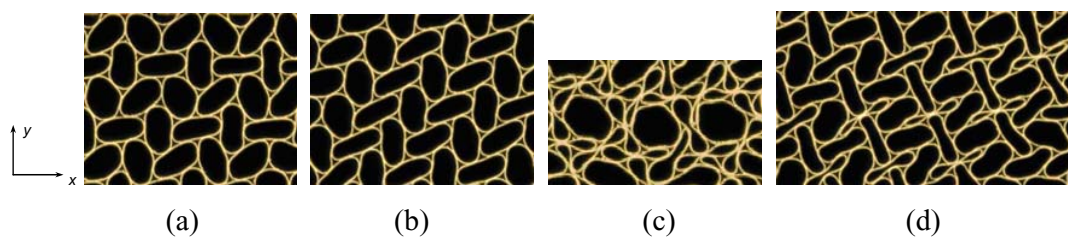


Figure 2

Accepted manuscript

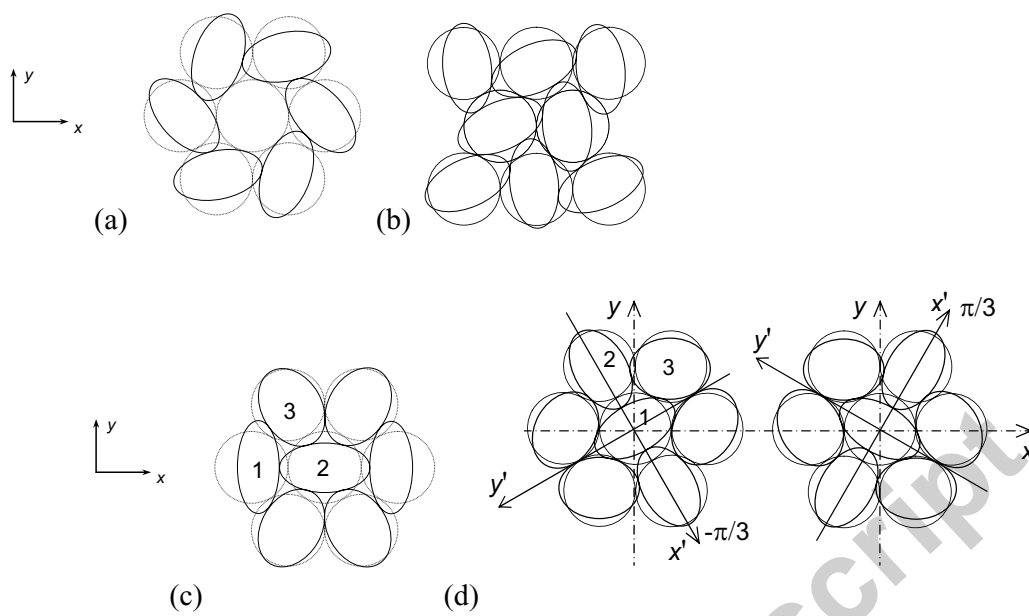


Figure 3

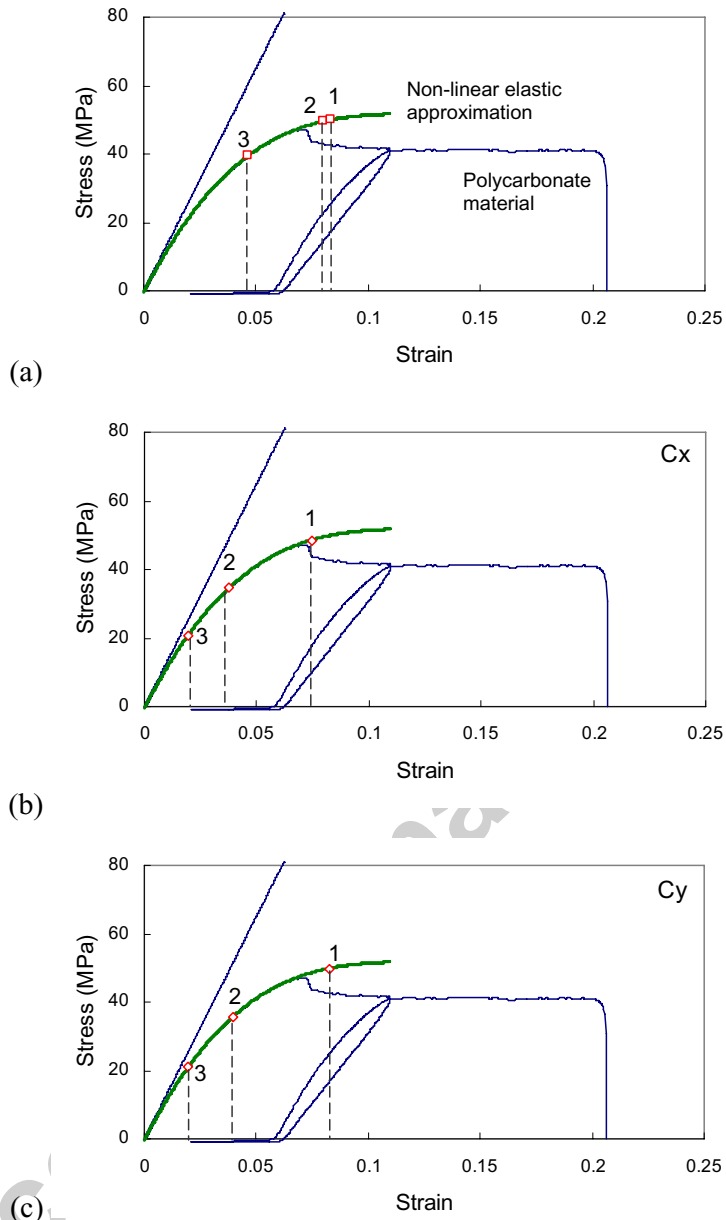


Figure 4

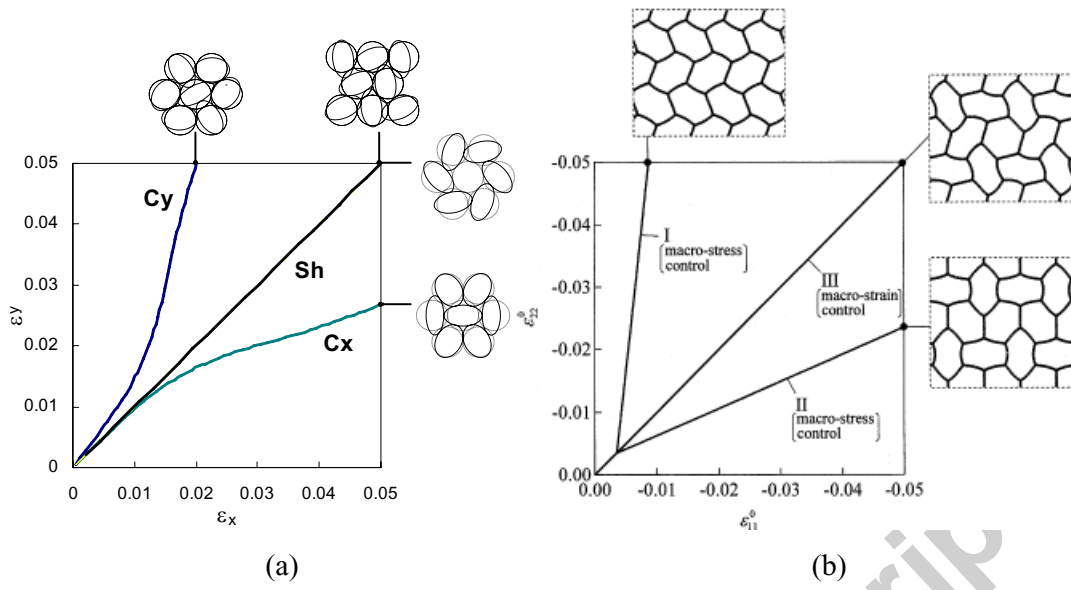


Figure 5

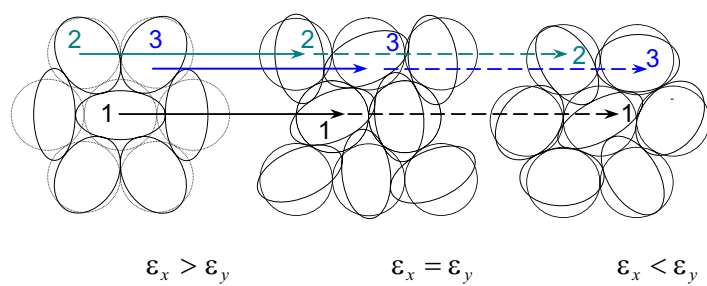


Figure 6

Accepted manuscript

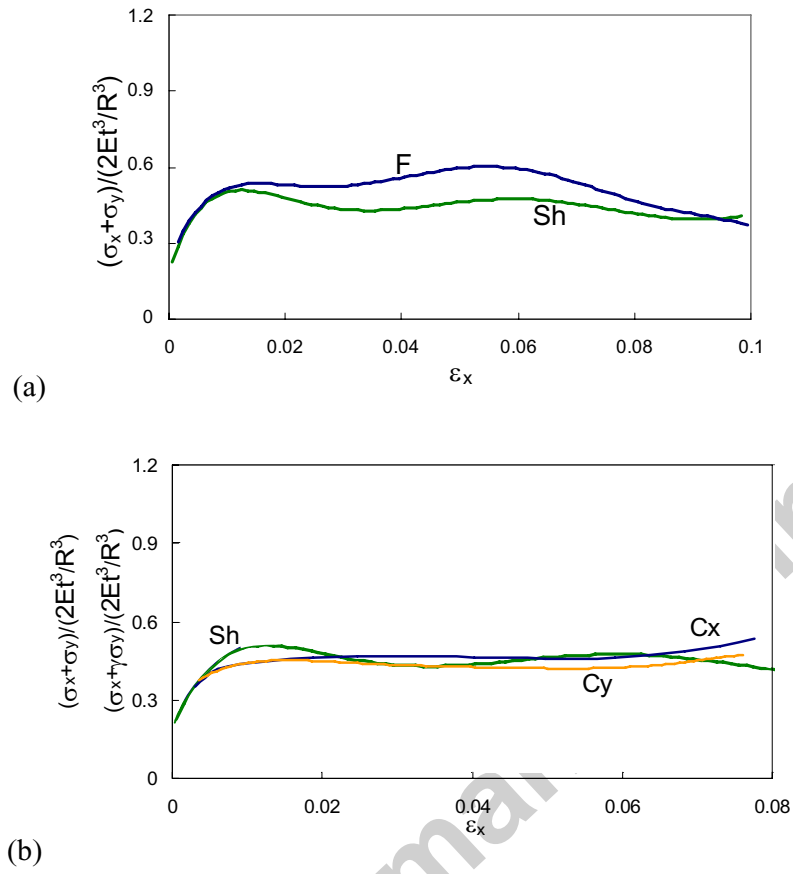


Figure 7

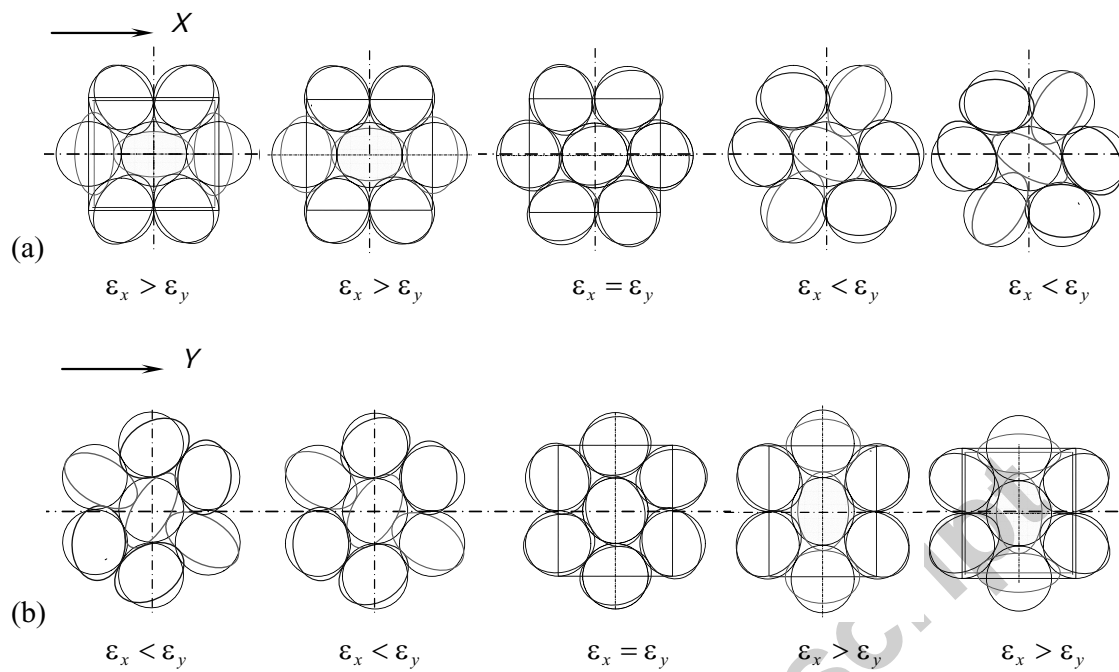


Figure 8

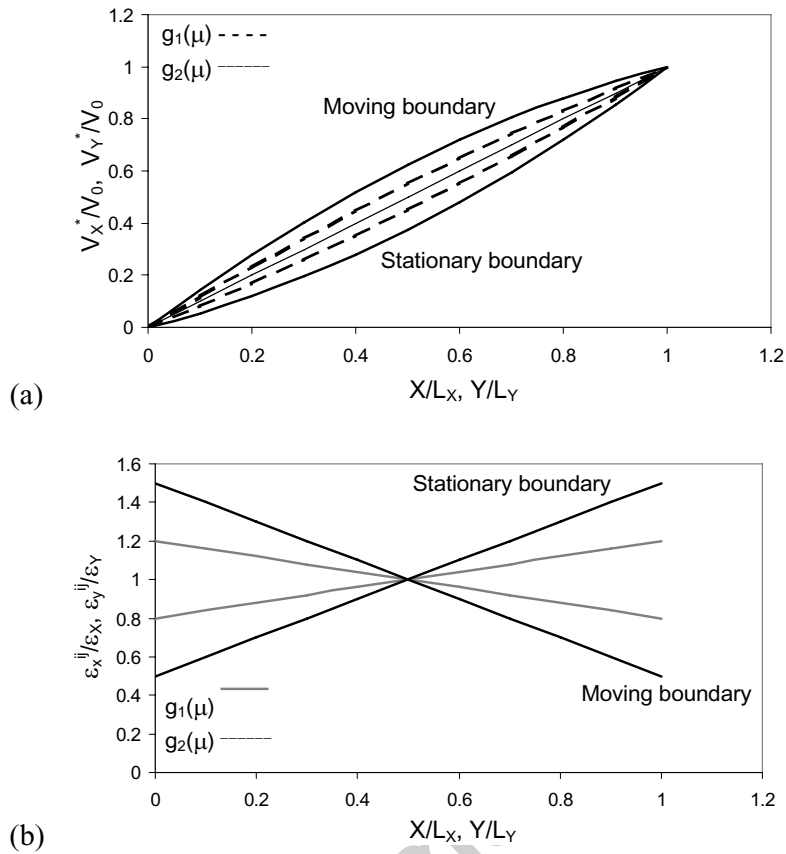


Figure 9

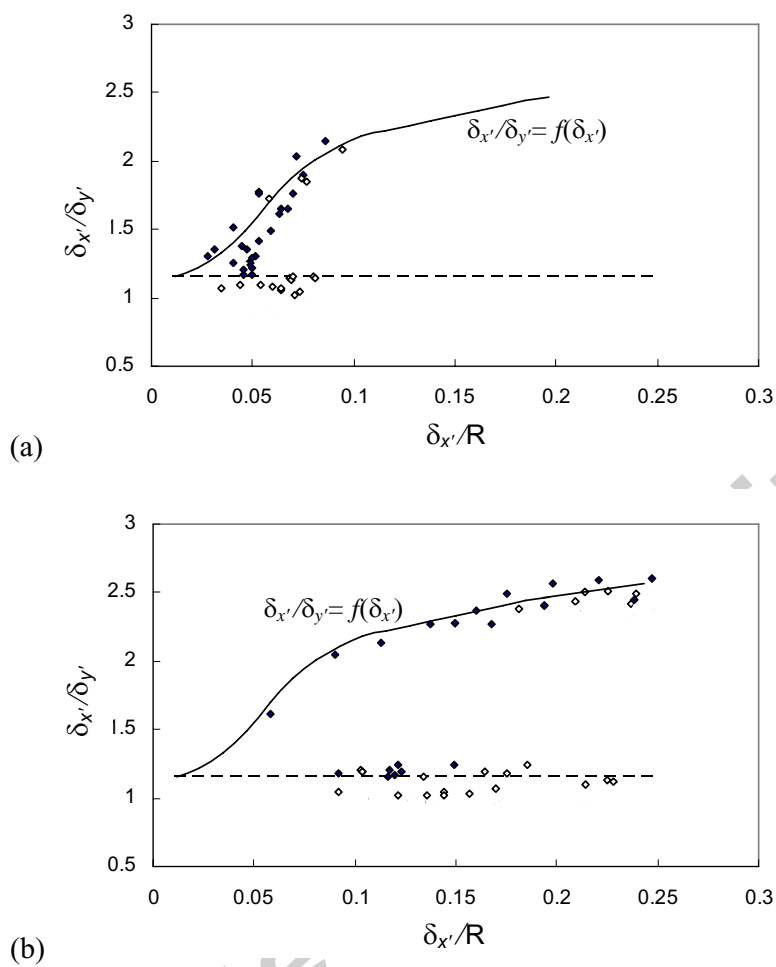


Figure 10

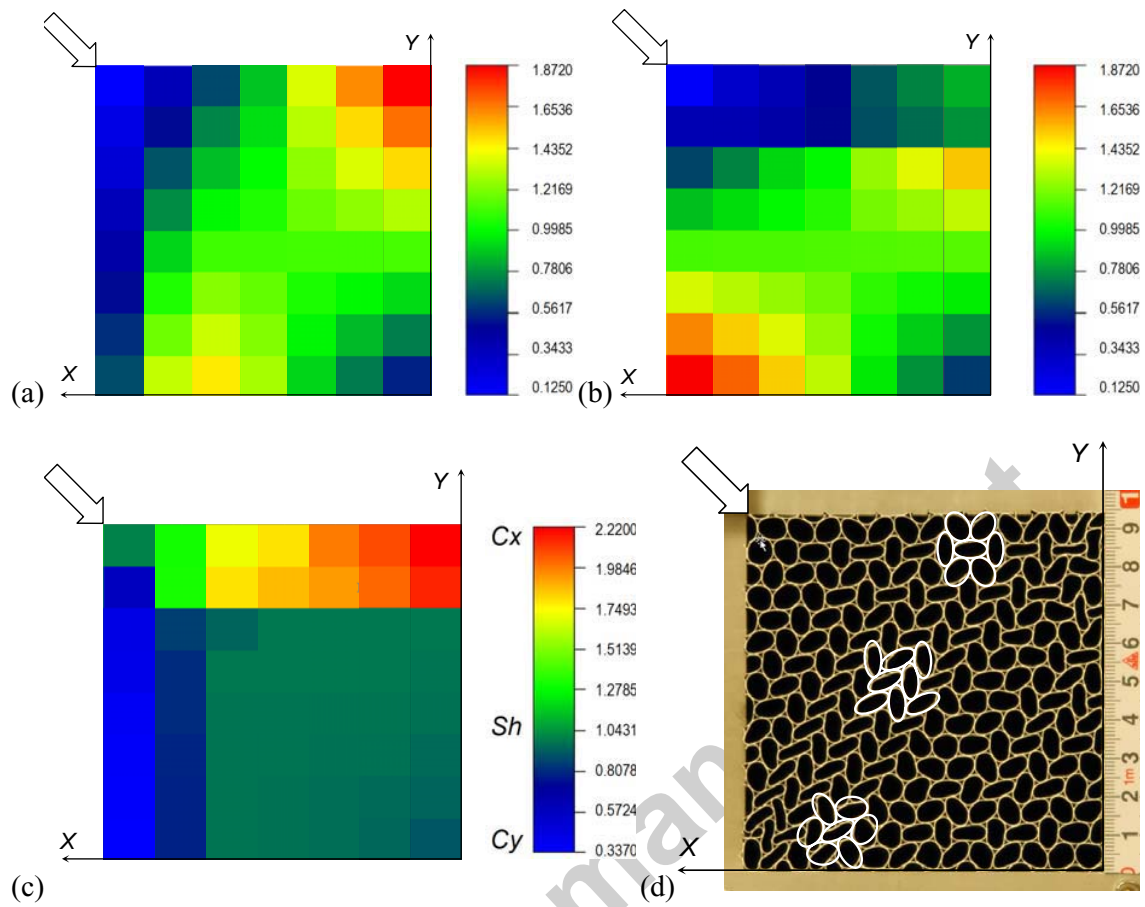


Figure 11

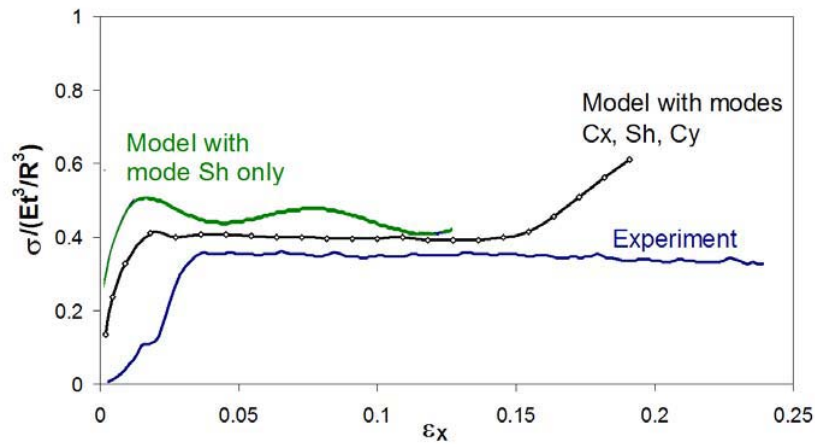


Figure 12

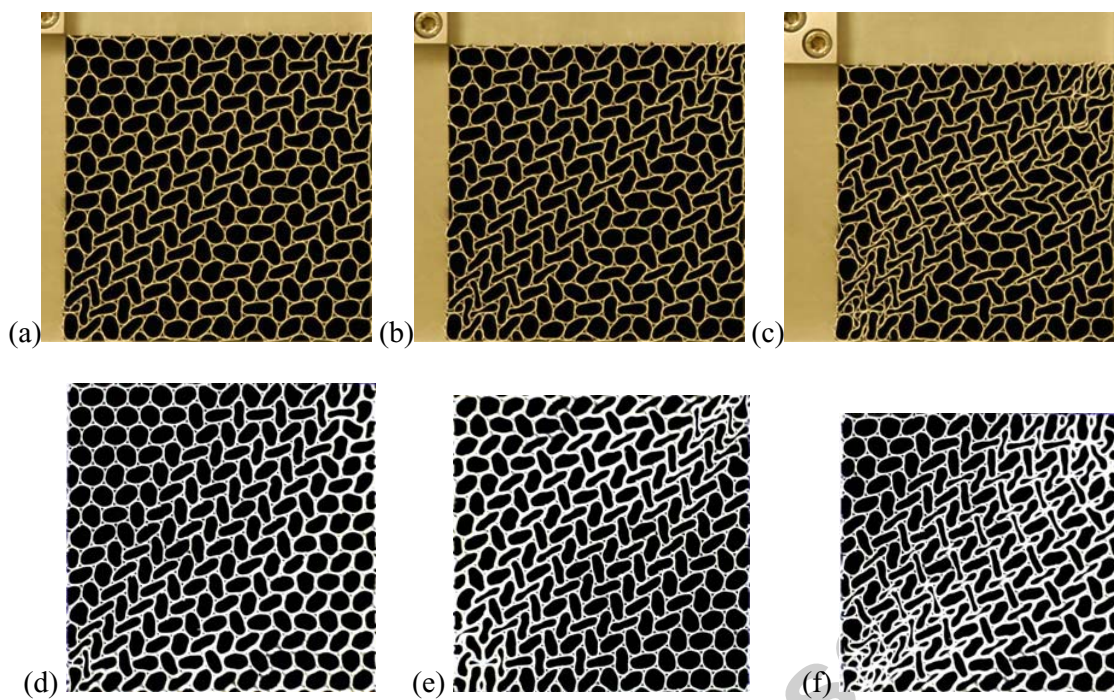


Figure 13

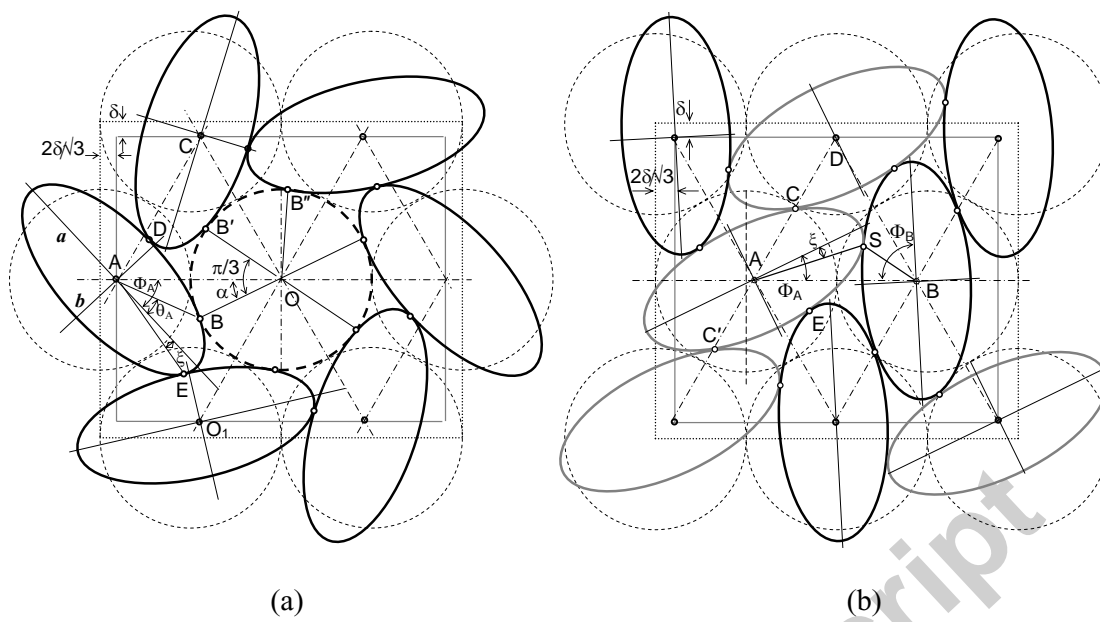


Figure A1

Accepted manuscript

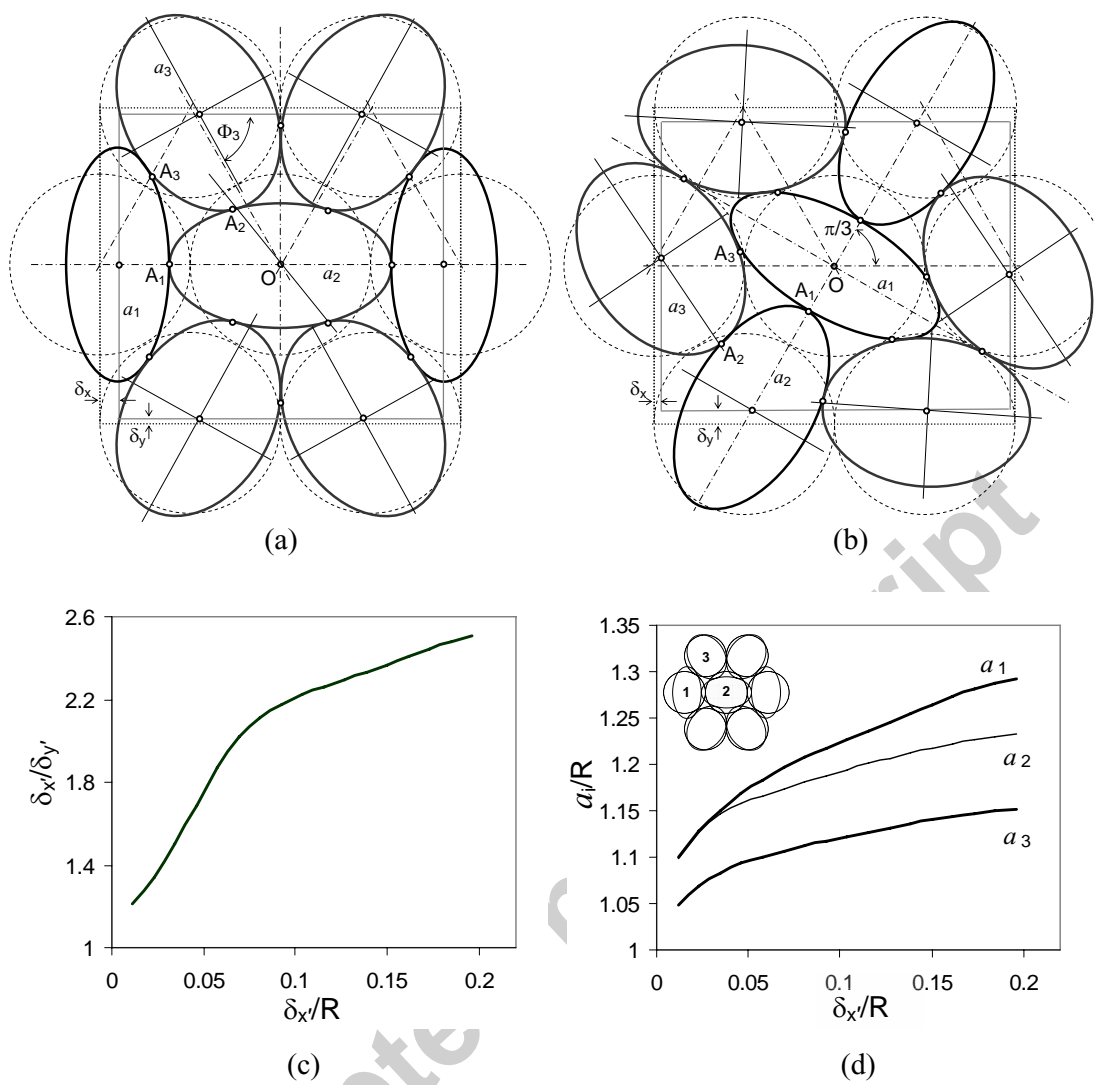


Figure A2

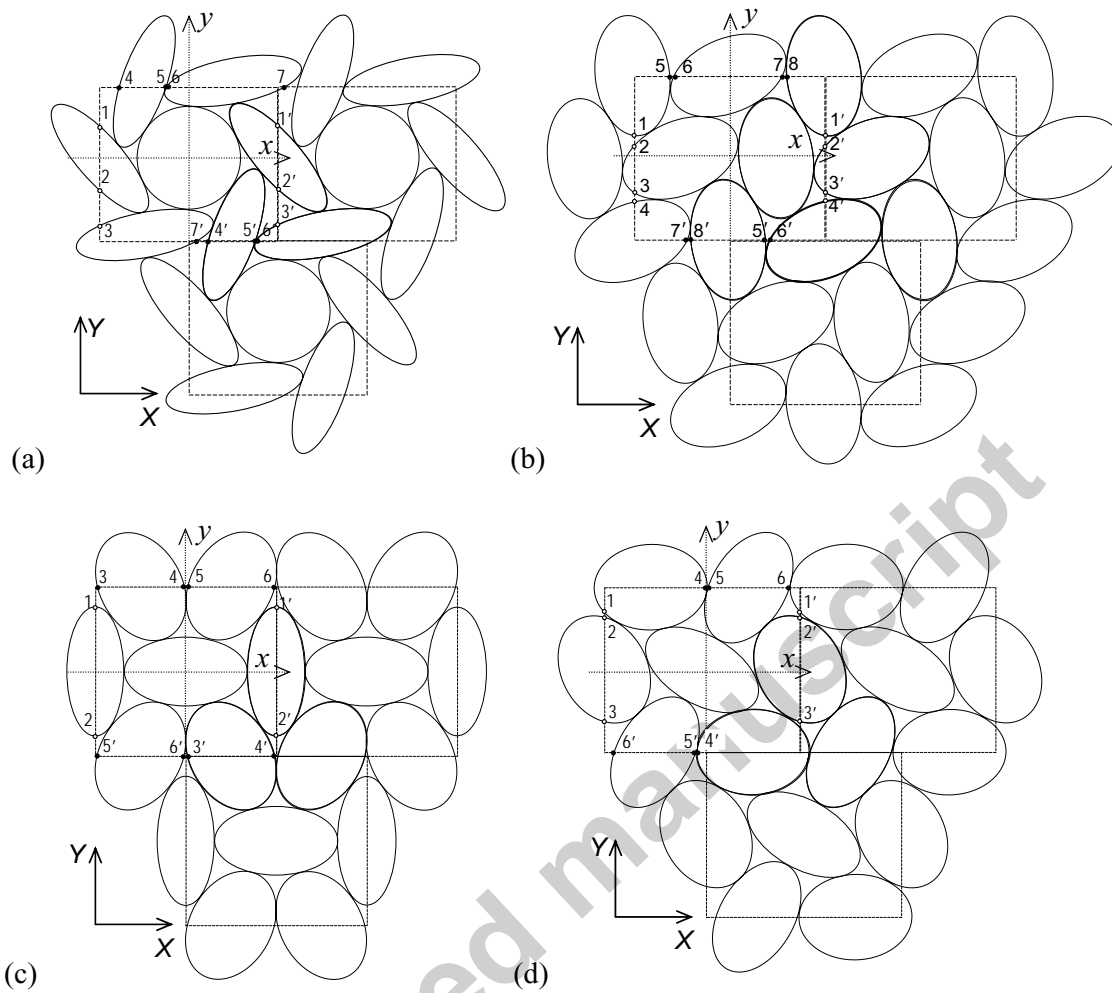


Figure A3